LLNL-JRNL-409414

Refraction-Enhanced X-ray Radiography for Inertial Confinement Fusion and Laser-Produced Plasma Application

J. A. Koch, O. L. Landen, B. J. Kozioziemski, N. Izumi, E. L. Dewald, J. D. Salmonson and B. A. Hammel

December 15, 2008

Journal of Applied Physics

This document was prepared as an account of work sponsored by an agency of the United States government. Neither the United States government nor Lawrence Livermore National Security, LLC, nor any of their employees makes any warranty, expressed or implied, or assumes any legal liability or responsibility for the accuracy, completeness, or usefulness of any information, apparatus, product, or process disclosed, or represents that its use would not infringe privately owned rights. Reference herein to any specific commercial product, process, or service by trade name, trademark, manufacturer, or otherwise does not necessarily constitute or imply its endorsement, recommendation, or favoring by the United States government or Lawrence Livermore National Security, LLC. The views and opinions of authors expressed herein do not necessarily state or reflect those of the United States government or Lawrence Livermore National Security, LLC, and shall not be used for advertising or product endorsement purposes.

Refraction-Enhanced X-ray Radiography for Inertial Confinement Fusion and Laser-Produced Plasma Applications

Jeffrey A. Koch, Otto. L. Landen, Bernard J. Kozioziemski, Nobuhiko Izumi,

Eduard L. Dewald, Jay D. Salmonson, Bruce A. Hammel

Lawrence Livermore National Laboratory

P. O. Box 808, L-481, Livermore, California, 94551

Abstract

We explore various laser-produced plasma and inertial-confinement fusion (ICF) applications of phase-contrast x-ray radiography, and we show how the main features of these enhancements can be considered from a geometrical optics perspective as refraction enhancements. This perspective simplifies the analysis, and often permits simple analytical formulae to be derived that predict the enhancements. We explore a raytrace approach to various material interface applications, and we explore a more general example of refractive bending of x-rays by an implosion plasma. We find that refraction-enhanced x-ray radiography of implosions may provide a means to quantify density differences across shock fronts as well as density variations caused by local heating due to high-Z dopants. We also point out that refractive bending by implosions plasmas can blur fine radiograph features, and can also provide misleading

contrast information in area-backlit pinhole imaging experiments unless its effects are taken into consideration.

I. Introduction

Phase-contrast imaging has a long history as an optical and x-ray radiography technique. In the simplest implementations, image contrast for weakly-absorbing phase objects can be understood to arise from diffraction across transverse phase gradients. More sophisticated techniques include Zernike phase-contrast imaging [1, 2], which has been extended to the x-ray regime using both Fresnel zone plates [3] and refractive bubble lenses [4].

In general, analysis of phase-contrast imaging requires a wave optics treatment based on scalar diffraction theory [5]. However, in many cases of interest, the main features of phase-contrast x-ray images can be understood from a geometrical optics perspective. We will show that this often allows simple analytical formulas to be derived that can predict the results of experiments and how the results scale with various parameters.

In this paper, we explore a variety of phase-contrast imaging applications of particular interest to laser-produced plasma research and inertial confinement fusion (ICF). We show that in these applications, the most important phase contrast effects can indeed be understood from a geometrical optics perspective and can be modeled with raytracing.

II. Diffraction Theory and Geometrical Optics

The starting point for analysis of diffraction features in images is usually Fresnel-Kirchoff scalar diffraction theory, and we present an example problem in Fig. 1. Here, a plane wave incident from the left illuminates a slit in a tilted block of high-index material with depth L, and we are interested in calculating the intensity pattern at the back of the block. The complex electric field in this plane is given by the integral [5],

$$E(y) \propto \int_{aperture} \frac{K(\theta)}{r} \exp\left(ikx + iknr - \pi/2\right) \tag{1}$$

where r is the distance along a ray path from the aperture point $(x, x/\tan\theta_i)$ to the image point (L, y), θ is the angle this ray path makes with respect to the x axis, k is the wavenumber $2\pi/\lambda$, n is the real part of the index of refraction of the block, and $K(\theta)$ is an obliquity factor $(\cos\theta+1)/2$. Eq. (1) is only valid in the limit $r >> \lambda$, but is otherwise quite general; the light intensity at the point y is $I(y) \propto E(y)E^*(y)$. This is simply a mathematical representation of Huygen's principle; a scalar diffraction calculation of the intensity profile for this example is shown in Fig. 1.

In the geometrical optics limit, we effectively replace $K(\theta)$ by a delta function $\delta(\theta - \theta_t)$, where we find θ_t from Snell's law $\sin\theta_i = n\sin\theta_t$. This collapses the integral over many possible paths to a single ray path corresponding to the path of minimum time. An analytical calculation of this simplified intensity profile is also shown in Fig. 1, and agrees well with the diffraction calculation. Strictly speaking, the geometrical optics limit corresponds to the Fresnel number $F \approx a^2/f\lambda >> 1$, where a is the characteristic feature dimension, 1/f = 1/object

distance p + 1/image distance q, and λ is the light wavelength [6, 7]. However, we show in the following sections that for many applications relevant to laser-produced plasma research, we can use geometrical optics to calculate the most important features of phase-contrast images even with Fresnel numbers $F \sim 1$. We refer to phase-contrast imaging in this regime as refraction-enhanced imaging [8]. This simplified treatment is powerful because it allows simple analytical scaling formulas to be derived for various cases of interest, and allows numerical raytracing to be used to simulate image features that would otherwise require a full diffraction treatment. Similar geometrical optics simplifications have been utilized to calculate the focusing properties of curved, variable-line-spacing, and radial diffraction gratings [9 - 11], where in these cases the grating equation replaces Snell's law.

III. Refraction-enhanced imaging of surfaces

The first example we explore is face-on radiography of a sinusoidal ripple in a weakly-absorbing planar substrate. This geometry is typically utilized to measure instability growth in laser- or x-ray-driven planar [12] and converging [13] samples. We consider the case of a plane wave incident onto the rippled surface of a thin substrate with index of refraction n, having a surface equation $y = A\cos(kx)$. We use a small-angles approximation to find the angle of incidence,

Snell's law to find the transmitted angle, and Snell's law again to find the final deviation angle,

$$\theta_i = Ak\sin(kx) \tag{2}$$

$$\theta_t = \frac{Ak}{n}\sin(kx) \tag{3}$$

$$\theta_f = Ak(1-n)\sin(kx) \tag{4}$$

The final position of the ray on the detector at distance q is,

$$x_f = x - Akq(1-n)\sin(kx) \tag{5}$$

If the initial beam intensity is I_0 = N/dx, the final image plane intensity is I_f = N/dx_f, where,

$$dx_f = dx(1 - Ak^2q(1-n)\cos(kx)) \tag{6}$$

$$I_f = I_0(1 + Ak^2q(1-n)\cos(kx)) \tag{7}$$

The image plane contrast C = (I_{max} - I_{min})/(I_{max} + I_{min}) is then,

$$C = Ak^2q(1-n) = q\Delta n\frac{d^2y}{dx^2} \tag{8}$$

For x-ray energies well above any absorption edges, the index of refraction of a material is approximately given by [14],

$$n = 1 - \frac{N_e r_0 \lambda^2}{2\pi} \tag{9}$$

where N_e is the electron density, r_0 is the classical electron radius, and λ is the x-ray wavelength. It can be shown that for a finite source distance p, we can replace q in eq. (8) by f, where 1/f = 1/p + 1/q. We see therefore that,

$$C \propto f\lambda^2 N_e \frac{d^2 y}{dx^2} \tag{10}$$

when the second derivative is well-defined, which is apparently a general result [15] for small perturbations. Fig. 2 shows simulated phase-contrast diffraction projections for a variety of realistic sinusoidal perturbations in a plastic substrate, compared with the predictions from eq. (8). We find good agreement (better than 40%) that improves when the contrast reduces. For this example, feature sizes on the order of 10 μm result in Fresnel numbers on the order of 1, so eq. (8) is a reasonable approximation.

The next example we explore is face-on x-ray radiography of a cusp-like groove in the inner surface of a deuterium-tritium (DT) ice layer inside a spherical beryllium capsule [15, 16]. This is a key application for metrology of DT ice surfaces, which is important for the purposes of achieving ignition at the National Ignition Facility [17, 18]. X-ray radiography is necessary since the Be shell is opaque to visible light, and since x-ray absorption in hydrogen ice is negligible, all information obtained about the DT ice layer derives from refraction enhancements. The most important surface defects in DT ice layers are believed to be grain boundary grooves between regions of the ice surface with slightly different crystal structure, and these grooves are predicted to have an analytical profile approximated by [19],

$$y = \frac{A}{\left(1 + \frac{|x|}{w}\right)^2} \tag{10}$$

From eq. (8), the expected refraction-enhanced contrast for an infinite object distance is,

$$C = 6\frac{A}{w^2}q(1-n) \tag{11}$$

Fig. 3 shows simulated phase-contrast diffraction projections for a variety of cusp profiles in a DT ice substrate, compared with the predictions from eq. (11). The sharp cusp tip generates subsidiary maxima and minima that cannot be derived from a geometrical optics treatment, but we still find approximate agreement (factors of a few) with the prediction from eq. (11). For this example, feature sizes on the order of 3 μm result in Fresnel numbers on the order of 1, but the infinitely sharp cusp generates a range of size scales so we would expect eq. (11) to be a crude approximation to the full diffraction solution.

A third example is radiography of the limb of a DT ice surface inside an ICF capsule [15, 16]. The inner surface of the DT ice layer is made visible in x-ray radiographs by refraction enhancements, and local variations in the ice radius due to surface perturbations can be diagnosed by changes in the apparent radius of the edge in the radiograph, in a manner similar to backlit optical imaging of ice layers in transparent shells [20, 21]. We explore this example in detail because it is an especially important ICF application of refraction-enhanced imaging, and because the resulting analytical expressions are valuable for scaling current radiography systems to other sources having different x-ray energies and sizes, as we discuss below.

We first consider the case of a solid sphere or cylinder of refractive index n_1 and radius R imbedded in a second material of lower refractive index n_2. We ignore absorption and show later that reflection is negligible and that diffraction can be neglected for ICF targets of interest. A ray arriving at an angle α to the interface refracts an internal angle β, then exits by symmetry at the same angle α□□□□□□□ig.□4□. By Snell's law, $n_1/n_2 = \cos\alpha/\cos\beta \approx 1 - \alpha^2/2 + \beta^2/2$. Therefore, $\Delta n/n \approx \Delta n \approx (\beta^2 - \alpha^2)/2 \approx \alpha(\beta - \alpha)$ since $n \approx 1$ for x-rays and $\beta \approx \alpha$ for relevant values of α that dominate the refraction signature, as will be shown below. The total bending angle entering and exiting is then,

$$\theta = 2(\beta - \alpha) \approx 2\Delta n/\alpha \tag{12}$$

Rays arriving most tangentially (with lowest α) bend most, as shown in Fig. 4. This leaves a dark band (or dark fringe) followed by an excess of signal (or light fringe) in the projected image. For any given ray traveling a distance p to the object plane and a further distance q past the object, we define transverse object, refraction and projected image impact parameters as o, r and i, respectively, relative to the tangential ray, where positive impact parameter is towards the object center. The width of the dark band is then simply the minimum value of the projected image impact parameter i. By Fig. 4, the object impact parameter $o = R(1 - \cos\alpha) \approx R\alpha^2/2$. Substituting for α□□□□e□.□□□2□, we have,

$$\theta \approx \frac{r}{q} = \Delta n\sqrt{\frac{2R}{o}} \tag{13}$$

Using eq. (13), the projected image impact parameter i as a function of positive object impact parameter o is then given by geometry (see Fig. 4) in the limits R << q as,

$$i = \left(\frac{p+q}{p}\right)o + r = \left(\frac{p+q}{p}\right)o + q\Delta n\sqrt{\frac{2R}{o}} \tag{14}$$

Fig. 5 shows the normalized fringe strength ~ do/di plotted against normalized impact parameter i. The dark fringe width (i.e. the minimum value i_c) is found by differentiating i with respect to o using eq. (3) and setting the result equal to zero, yielding,

$$o_c = \left(\frac{pq\Delta n\sqrt{\frac{R}{2}}}{p+q}\right)^{2/3} = \left(f\Delta n\sqrt{\frac{R}{2}}\right)^{2/3} \tag{15}$$

$$i_c = 3q\left(\frac{1}{f}\right)^{1/3}\left(\Delta n\sqrt{\frac{R}{2}}\right)^{2/3} \tag{16}$$

where f is defined above eq. (10).

We now consider the effect of finite point source size s in the limit of high magnification projection radiography from a point source (q >> p). The blurring due to a finite source size can be simply visualized by rotating all the rays in Fig. 4 about the center of the sphere, so that the rays appear to emanate from a different point on the source. Equating this magnified blurring $s_c(q/p)$ to the dark fringe width at the projected image plane (eq. (16)), we find that,

$$s_c = 3\left(p\Delta n\sqrt{\frac{R}{2}}\right)^{2/3} = 3o_c \tag{17}$$

Conveniently, if we set q and R in units of cm and Δn in units of 10^{-6}, then s_c is in units of μm. With typical values p = 6 cm, $\Delta n \approx n_e/2n_c \approx 3\text{x}10^{-6}$ (for solid matter electron density $N_e = 3\text{x}10^{23}$ cm^{-3} and 8 keV x-ray critical density $N_c \approx 10^{29}$ cm^{-3}) and R = 0.1 cm, eq. (17) yields s_c = 10 μm, a viable point projection laser plasma source size [22 - 24]. Furthermore, by eqs. (12), (13) and (15), θ_c = 85 μrad and α_c = 70 mrad, proving that the bending angle θ_c that determines the width of the dark fringe is indeed much less than the incident grazing angle α_c, thereby validating eqs. (12 - 17).

The case just presented is applicable for refraction at the DT ice/gas and DT ice/ablator interfaces of an ICF capsule, where the outside material has higher electron density and lower x-ray refractive index. We now consider the reverse case of a solid sphere of refractive index n_1 and radius R imbedded in a second material of lower density and higher x-ray refractive index n_2, such as a sphere in vacuum or air. In this case, as shown in Fig. 6, there will be no completely dark band as for the positive Δn case. Instead, a brighter and a dimmer fringe will extend from the negative and positive side of i = 0. Eq. (14) still holds with Δn now negative rather than positive. Fig. 7 depicts the normalized fringe strength ~ do/di against the normalized image impact parameter i. Interestingly, the fringe contrast in the absence of any source size blurring is now a constant, (5/3)/(2/3) = 2.5. Equating the magnified source blurring $s_c(q/p)$ to either the FWHM of the bright or dark

fringe shown in Fig. 7 leads to the same source size limits as eq. (6) to within factors of $1/2^{2/3}$ or $1/5^{1/3}$.

We now compare the relative importance of refraction vs. reflection at a perfect cylindrical interface by comparing the magnitude of the object impact parameters defining each effect. The maximum impact parameter o_{crit} for total external reflection is found by setting the internal ray angle $\beta = 0$, which leads to a critical incidence angle $\alpha_{crit} = (2\Delta n)^{0.5}$ and hence $o_{crit} \approx R\alpha_{crit}^2/2 \approx R\Delta n$. This is a few nm compared to a few μm for o_c (eq. (17), and therefore reflection is negligible.

Finally, we compare the relative fringe scales for refraction and diffraction. If we consider the previous high magnification point projection case, the first Fresnel diffraction fringe size [25] is $h_c = (p\lambda)^{0.5} = 3$ μm, compared with eq. (16) $i_c = 1.3q$ μm. Since by definition $q >> p = 6$ cm, i_c will be much greater than 8 μm, and therefore much greater than h_c. Since $h_c \sim \lambda^{1/2}$ while $i_c \sim \lambda^{4/3}R^{1/3}$, both types of fringe widths will decrease as the x-ray wavelength decreases, and diffraction should only replace refraction as the dominant scale fringe pattern at sufficiently short λ or for small enough objects [25 - 27]. Finally, from eq. (16), $\Delta i_c/i_c = 4/3(\Delta\lambda/\lambda$, confirming that source bandwidths as large as $\Delta\lambda \sim \lambda$ are acceptable in terms of fringe blurring [28].

Fig. 8 shows a simulated radiograph of a section of a Be shell, generated using a custom Monte Carlo raytracing code [20, 21], showing the refraction-enhanced edge features discussed above. In Fig. 9 we compare the simulated inner dark band, outer dark band, and outer peak band widths to analytical predictions scaled back to

the object plane, where the results are independent of imaging magnification; these are explicitly,

$$W_{inner} = 3\left(f\Delta n\sqrt{\frac{R}{2}}\right)^{2/3} \tag{18}$$

$$W_{outer}^{dip} = \frac{3}{5^{1/3}}\left(f\Delta n\sqrt{\frac{R}{2}}\right)^{2/3} \tag{19}$$

$$W_{outer}^{peak} = \frac{3}{2^{2/3}}\left(f\Delta n\sqrt{\frac{R}{2}}\right)^{2/3} \tag{20}$$

We find excellent agreement between the analytical predictions and the simulation results. We note that our ability to quantify surface perturbations along the limb of x-ray radiograph images has been validated by independent measurements of surface perturbations on the outside surface of a surrogate shell [29], and this in turn validates a geometrical optics treatment of the problem for perturbation mode numbers as high as ~ 100 and perhaps higher. This is useful because it allows raytracing software to be utilized to simulate x-ray radiographs of complex surface structure in thick objects that would otherwise require a multi-slice diffraction simulation [30]. Fig. 10 shows a comparison of a radiograph of a bumpy solid sphere with a simulated raytrace radiograph of a bumpy sphere having a comparable surface power spectrum and ~ μm-scale peak-to-valley heights, generated with a custom raytracing code [20, 21]. The visible surface structures in the experimental image can be understood as refraction enhancements, and are

particularly pronounced near the limb where the angles of incidence are most grazing.

Finally, application of the above analytical equations for refraction-enhanced radiography of shells allows current experimental geometries (typically 8 keV point-projection from a ~ 5 μm source [15]) to be scaled to other sources having different x-ray energies and sizes. Fig. 11 shows an experimental radiograph of a thin plastic shell generated by a ~ 100 μm-diameter laser-produced Au plasma x-ray source, in a low-magnification (near-contact radiography) geometry using x-ray film as a detector. This source was filtered to pass primarily M-band radiation in the 2.5 - 4 keV spectral range, and the geometry was determined using eq. (18) and straightforward photometric calculations. The refraction enhancements are clearly visible on the inside edge of the shell, and faintly visible on the outside edge.

IV. Refraction-enhanced imaging of implosion plasmas

The examples we discussed in Section III all relate to refraction enhancements due to material interfaces. Another area where refraction enhancements may prove useful in future experiments is in detection and quantitative analysis of density gradients in implosion plasmas. The geometry is shown in Fig. 12, and we are interested in calculating the deflection angle of a ray passing through the plasma from a distant backlight. For all ray paths, we have [5],

$$n(r)r\sin\phi = b \tag{21}$$

which results in two equivalent equations,

$$\theta(r) = b\int^{r} \frac{dr}{r\sqrt{n(r)^2 r^2 - b^2}} \tag{22}$$

$$\frac{dy}{dx} = \pm\left(\arctan\left(\frac{b}{\sqrt{n(r)^2 r^2 - b^2}}\right) - \arctan\left(\frac{y}{x}\right)\right) \tag{23}$$

with the latter eq. (23) being more convenient for numerical solutions. A particularly simple case is $n(r) = 1+(r_0/r)^2$, for which an analytical solution for the total deflection angle δ is,

$$\delta = \frac{\pi}{4} b\left.\frac{dn}{dr}\right|_b \approx b\left.\frac{dn}{dr}\right|_b \propto b\left.\frac{dN_e}{dr}\right|_b \tag{24}$$

This suggests that in general the total deflection angle will be approximately equal to the impact parameter b times the gradient in the index of refraction at r = b. Since the index of refraction is proportional to the electron density Ne, the deflection angle is proportional to the density gradient; this in turn suggests that refraction enhancements in radiographic images can provide direct information about Atwood numbers ($\Delta\rho/\rho$) across shock fronts [12, 13], and this would be valuable in evaluating the sensitivity to growth of Rayleigh-Taylor instabilities during implosion experiments.

A simulated density profile of a model NIF implosion is shown in Fig. 13 [32]. The Be capsule has converged by a factor of two from an initial radius of 1 mm, and during the implosion the density profile near the peak has evolved to

show several zones of higher and lower density; a sharp interface across the boundary between the shell and the DT ice, and several shallow density dips in the shell material that are caused by preferential heating of Cu-doped Be regions [33]. Using the simulated density profile, we can use eq. (23) to calculate the expected deflection angles in a radiography experiment, and these deflections are plotted in Fig. 14 for an 8.4 keV backlighter energy. We find deflections as large as ~ 200 μ-radians, with the shell/ice interface visible as a sharp discontinuity in the deflection vs. radius and with the Cu dopant zones also visible.

We can use the deflection plot of Fig. 14 to generate simulated radiographs at various values of f (source distance at high magnification, detector distance at low magnification), under the assumption that absorption contrast variations are negligible and for perfect spatial resolution. Fig. 15 shows histogram intensity profiles from a Monte Carlo raytrace, for several values of f. We see that when f is small (1 - 10 mm), the shell/ice interface is clearly evident as a high-contrast but narrow (~ 1 μm) dark band. We can estimate the expected width by treating the interface as infinitely sharp and using the density plot in Fig. 14 together with eq. (18) with f = 5 mm, and this analytical estimate (1.2 μm) is in good agreement with the simulation.

As f increases (Fig. 15), the width of the dark band increases but the contrast degrades as x-rays refracted from different regions of the plasma by different amounts coalesce, and the dark band is eventually filled in by this

blurring at the same time the contrast of the Cu-doped Be regions increases. Fig. 16 show how the limiting case is eventually realized where a wide dark band forms in the radiograph and all fine structure is lost. In this limit, the width of the dark band is set by the average density of the shell material relative to vacuum. For this particular case, we performed a diffraction simulation of the same problem, and found good agreement with the raytrace (Fig. 16(c)). Using eqs. (18 - 19), we would predict a width of ~ 80 μm, again in good agreement with the simulation.

V. Summary

We have shown that in many cases of interest to laser-produced plasma and ICF research, the main features of phase-contrast enhancements of x-ray radiography can be understood from a geometrical optics perspective and can be thought of as refraction-induced enhancements. This perspective simplifies the analysis, and often permits simple analytical formulae to be derived that predict these enhancements. We have shown how accurate analytical formulae can be obtained to predict refraction contrast in rippled substrates and in DT ice surfaces having grain-boundary grooves, and have explored how edge enhancements of shells can be understood through refraction-based analytical formulae that scale to different types of sources including relatively large laser-produced plasma backlighters used in low-magnification radiography. We have

also shown how refraction-based raytracing can be applied to these problems, and can be extended to rough surfaces.

We have shown how refraction-enhanced imaging is capable in principle of detecting and quantifying density modulations in NIF implosions, and have pointed out that analysis of refraction enhancements can provide information about Atwood numbers across shocks. However the range of values of f where this measurement is possible is limited, and while larger values of f increase the refraction enhancements, they also result in refractive blurring that eventually erodes contrast. We find in particular that the DT ice/shell interface in a NIF implosion may be made visible in a radiography experiment if < 1 μm resolution can be obtained in a f ~ 10 mm geometry and if a ~ ps-duration backlight [34] is used to minimize motion blurring. Alternatively, we can expect to measure the average density of the imploding shell and fuel with 5-10 μm resolution and larger (~ 50 mm) values of f.

Refractive blurring effects generally should be assessed in the interpretation of implosion radiography experiments even in an absorption-dominated regime. Pinhole imaging with a large area backlight source will eliminate refraction blurring, but in this case the refraction effects manifest themselves as changes in image contrast. This is because different parts of the plasma focus and defocus the backlight x-rays, as atmospheric gradients do in a time-dependent fashion to starlight leading to intensity variations (twinkling).

The pinhole blocks rays that have been deflected out of the aperture, so effects on the image intensity will begin to occur when the deflection angle (eq. (24)) equals the angle subtended by the pinhole viewed from the object. Using eqs. (9) and (24), we can estimate the maximum pinhole distance to avoid this as,

$$p_{\max}[mm] \approx \frac{11.1 d[\mu m]\Delta r[\mu m]}{b[\mu m]\lambda^2[\mathring{A}]\Delta N_e[10^{25} cm^{-3}]} \tag{25}$$

where d is the pinhole diameter. For the example in Fig. 13 at 8.4 keV, this is approximately 2 mm, very close for pinhole imaging of an implosion. Refractive effects should therefore be assessed before contrast differences in radiographs are interpreted as being caused by straight-ray differences in absorption.

This work was performed under the auspices of the U.S. Department of Energy by Lawrence Livermore National Laboratory under contract DE-AC52-07NA27344.

References

[1] F. Zernike, "Phase-contrast, a new method for microscopic observation of transparent objects, Pt. 1", Physica **9**, 686 (1942)

[2] F. Zernike, "Phase-contrast, a new method for microscopic observation of transparent objects, Pt. 2", Physica **9**, 974 (1942).

[3] M. Awaji, Y. Suzuki, A. Takeuchi, H. Takano, N. Kamijo, S. Tamura, M. Yasumoto, "Zernike-type X-ray imaging microscopy at 25 keV with Fresnel zone plate optics", J. Synchrotron Radiation 9, 125 (2002).

[4] Y. Kohmura, A. Takeuchi, H. Takano, Y. Suzuki, T. Ishikawa , "Zernike phase-contrast x-ray microscope with an x-ray refractive lens", J. De Physique. IV **104**, 603 (2003)

[5] *Principles of Optics, 2nd Ed.*, M. Born and E. Wolf (Pergamon, New York, 1964).

[6] S. Wang, E. Bernabeu, J. Alda, "Unified and generalized Fresnel numbers", Optical and Quantum Electronics **24**, 1351-1358 (1992).

[7] S. Wang, Q. Lin, L. Yu, X. Xu, "Fresnel number of a regular polygon and slit", Applied Optics **39**, 3453 (2000).

[8] K. Imamura, N. Ehara, K. Umetani, K. Miyamoto, Y. Kanemaki, K. Uesugi, Y. Inada, H. Ogata, Y. Nakajima, M. Fukuda, "Sensitive detection of voids in solid materials by refraction-enhanced synchrotron radiation imaging", Appl. Phys. Lett. **81**, 2559 (2002).

[9] J. A. Koch, "Compact high-resolution soft x-ray spectrograph design using two matched grazing-incidence gratings", Appl. Opt. **34**, 3693 (1995).

[10] J. H. Underwood, J. A. Koch, "High resolution tunable spectrograph for x-ray laser line width measurements using a plane varied line spacing grating", Appl. Opt. **36**, 4913 (1997).

[11] J. A. Koch, S. Cui, M. A. McNeill, "Effective focal length calculations and measurements for a radial diffraction grating", J. Opt. Soc. Am. A **16**, 2690 (1999).

[12] B. A. Remington, S. W. Haan, S. G. Glendinning, J. D. Kilkenny, D. H. Munro, R. J. Wallace, "Large growth, planar Rayleigh-Taylor experiments on Nova", Phys. Fluids B **4**, 967 (1992).

[13] D. K. Bradley, D. G. Braun, S. G. Glendinning, M. J. Edwards, J. L Milovich, C. M. Sorce, G. W. Collins, S. W. Haan, R. H. Page, R. J. Wallace, J. L. Kaae, "Very-high-growth-factor planar ablative Rayleigh-Taylor experiments", Phys. Plasmas **14**, 056313 (2007).

[14] B.L. Henke, E.M. Gullikson, J.C. Davis, "X-ray interactions: photoabsorption, scattering, transmission, and reflection at E=50-30000 eV, Z=1-92", Atomic Data and Nuclear Data Tables **54**(2), 181 (1993).

[15] D. S. Montgomery, A. Nobile, P. J. Walsh, "Characterization of National Ignition Facility cryogenic beryllium capsules using x-ray phase contrast imaging", Rev. Sci. Instruments **75**, 3986 (2004).

[16] B. J. Kozioziemski, J. A. Koch, A. Barty, H. E. Martz, Jr., W-K. Lee, K. Fezzaa, "Quantitative characterization of inertial confinement fusion capsules using phase contrast enhanced x-ray imaging", J. Appl. Phys. **97**, 063103 (2005).

[17] J. D. Lindl, "Development of the indirect-drive approach to inertial confinement fusion and the target physics basis for ignition and gain", Phys. Plasmas **2**, 3933 (1995).

[18] J. D. Lindl, P. Amendt, R. L. Berger, S. G. Glendinning, S. H. Glenzer, S. W. Haan, R. L. Kauffman, O. L. Landen, L. J. Suter, "The physics basis for ignition using indirect-drive targets on the National Ignition Facility", Phys. Plasmas **11**, 339 (2004).

[19] A. Chernov *et al.*, manuscript in preparation (2008).

[20] J. A. Koch, J. D. Sater, A. J. MacKinnon, T. P. Bernat, D. N. Bittner, G. W. Collins, B. A. Hammel, E. R. Mapoles, C. H. Still, "Numerical raytrace verification of optical diagnostics of ice surface roughness for inertial confinement fusion experiments", Fusion Science and Technology **43**, 55 (2003).

[21] J. A. Koch, J. Sater, D. Bittner, G. Collins, C. Geddes, Y. Lee, A. MacKinnon, "Quantitative analysis of shadowgraphy and transmission interferometry as diagnostics of hydrogen ice surface quality in ICF capsules", Fusion Technology **38**, 123 (2000).

[22] O. L. Landen, D. R. Farley, S. G. Glendinning, L. M. Logory, P. M. Bell, J. A. Koch, F. D. Lee, D. K. Bradley, D. H. Kalantar, C. A. Back, R. E. Turner, "X-ray backlighting for the National Ignition Facility", Rev. Sci. Instrum. **72**, 627 (2001).

[23] A. B. Bullock, O. L. Landen, D. K. Bradley, "10 and 5 μm pinhole-assisted point-projection backlit imaging for the National Ignition Facility", Rev. Sci. Instrum. **72**, 690 (2001).

[24] J. Workman, J. R. Fincke, P. Keiter, G. A. Kyrala, T. Pierce, S. Sublett, J. P. Knauer, H. Robey, B. Blue, S. G. Glendinning, O. L. Landen, "Development of intense point x-ray sources for backlighting high energy density experiments", Rev. Sci. Instrum. **75**, 3915 (2004).

[25] G. Margaritondo, G. Tromba, "Coherence-based edge diffraction sharpening of x-ray images: A simple model", J. Appl. Phys. **85,** 3406 (1999).

[26] A. Pogany, D. Gao, S. W. Wilkins, "Contrast and resolution in imaging with a microfocus x-ray source", Rev. Sci. Instrum. **68,** 2774 (1997).

[27] S. A. Pikuz, T. A. Shelkovenko, D. B. Sinars, K. M. Chandler, D. A. Hammer, "Phase contrast x-ray radiography using X-pinch radiation", Proc. SPIE **4504**, 234 (2001).

[28] A. G. Peele, K. A. Nugent, "Phase measurement using x rays", Rev. Sci. Instrum. **75**, 3382 (2004).

[29] E. Dewald, B. Kozioziemski, J. Moody, J. Koch, E. Mapoles, R. Montesanti, K. Youngblood, S. Letts, A. Nikroo, J. Sater, J. Atherton, "Benchmarking x-ray phase

contrast imaging for ICF DT ice characterization using roughened surrogates", Fusion Science and Technology (in press).

[30] H. E. Martz, Jr., B. J. Kozioziemski, S. K. Lehman, S. Hau-Riege, D. J. Schneberk, A. Barty, "Validation of radiographic simulation codes including x-ray phase effects for millimeter-size objects with micrometer structures", J. Opt. Soc. Am. A **24**, 169 (2007).

[31] N. Izumi, E. Dewald, B. Kozioziemski, O. L. Landen, J. A. Koch, "Development of a Laser-Produced Plasma X-ray source for Phase-Contrast Radiography of DT Ice layers", Fusion Science and Technology (in press).

[32] B. A. Hammel, M. J. Edwards, S. W. Haan, M. M. Marinak, M. Patel, H. Robey, J. Salmonson, "Simulations of high-mode Rayleigh-Taylor growth in NIF ignition capsules", Journal of Physics: Conference Series **112**, 022007 (2008).

[33] S. W. Haan, M. C. Herrmann, J. D. Salmonson, P. A. Amendt, D. A. Callahan, T. R. Dittrich, M. J. Edwards, O. S. Jones, M. M. Marinak, D. H. Munro, S. M. Pollaine, B. K. Spears, L. J. Suter, "Update on design simulations for NIF ignition targets, and the rollup of all specifications into an error budget", European Physical Journal D **44**, 248 (2007).

[34] Y. Kohmura, K. Okada, A. Takeuchi, H. Takano, Y. Suzuki, T. Ishikawa , T. Ohigashi, H. Yokosuka, "High spatial resolution hard x-ray microscope using x-

ray refractive lens and phase contrast imaging experiments", Nuc. Instrum. Meth. Phys. Research A **467-468**, 881 (2001).

[35] H.-S. Park, N. Izumi, M. H. Key, J. A. King, J. A. Koch, O. L. Landen, P. K. Patel, D. F. Price, B. A. Remington, H. F. Robey, R. A. Snavely, M. Tabak, R. P. J. Town, J. E. Wickersham, C. Stoeckl, M. Storm, W. Theobald, D. M. Chamber, R. Eagleton, T. Goldsack, R. J. Clarke, R. Heathcote, E. Giraldez, A. Nikroo, D. A. Steinman, R. B. Stephens, B. B. Zhang, "High-energy K-alpha radiography using high-intensity, short-pulse lasers", Phys. Plasmas **13**, 056309 (2006).

Figure Captions

Figure 1: Sketch illustrating wave and ray propagation through a tilted slit in front of a block of material with index n. Simulated intensity profiles at the back of the block are shown at right, for Fresnel diffraction (oscillatory curve) and geometrical optics (sharp-edged curve).

Figure 2: Intensity profile of a radiographed sine-wave surface perturbation in a plastic substrate, with Δn = 5.1e-5, λ = 4.96 Å, and f = 182 mm and various values of amplitude A and period $L = 2\pi/k$, compared with the analytical predictions from eq. (8).

Figure 3: Intensity profile of a radiographed cusp surface perturbation in a plastic substrate, with Δn = 5.8e-7, λ = 1.48 Å, and f = 66 mm and various values of amplitude A and half-width w, compared with the analytical predictions from eq. (11).

Figure 4: Refraction geometry for the case of a sphere having index n_1 that is greater than the outside index n_2.

Figure 5: Signal in units of $p/(p + q)$, versus projected image impact parameter i in units of $(p + q)/p$, setting for convenience $(p/(p + q))q\Delta n(2R)^{0.5} = 1$.

Figure 6: Refraction geometry for the case of a sphere having index n_1 that is less than the outside index n_2.

Figure 7: Signal in units of $p/(p + q)$ versus projected image impact parameter i in units of $(p + q)/p$, setting for convenience $(p/(p + q))q\Delta n(2R)^{0.5} = 1$.

Figure 8: Simulated radiograph of a section of a Be shell. The x-ray energy is 8.4 keV, the shell outer diameter is 2 mm, the shell thickness is 150 μm, and the source and detector distances are 75 mm and 675 mm.

Figure 9: Calculated inner dark band width (a), and outer dark band and outer peak widths (b) for the image in Fig. 8 (eqs. 18-20), compared with raytrace simulations.

Figure 10: Comparison of a radiograph of a bumpy solid sphere (a) with a simulated raytrace radiograph of a bumpy sphere having a comparable surface power spectrum and ~ μm-scale peak-to-valley heights, generated with a raytracing code (b).

Figure 11: 2-mm diameter plastic shell radiographed at low-magnification onto x-ray film by a Au laser-produced plasma backlight emitting primarily M-band radiation near 2.5 keV. The edge enhancements are due to refraction.

Figure 12: Geometry of beam steering in a density gradient. The ray with initial impact parameter b is incident from the left, and is deflected by a total angle δ.

Figure 13: Simulated density gradient in a NIF implosion of a Be shell surrounding a shell of solid DT fuel, at a time when the shell has converged by a factor of ~ 2. Annular regions of the shell are doped with

Cu, and regions as well as the shell/ice interface are visible in the density profile.

Figure 14: Deflection angle and density versus radius for the density profile shown in Fig. 13. The shell/ice interface and the Cu-doped regions cause changes in the beam deflections, and these deflections will affect radiographs.

Figure 15: Simulated radiographs through the density profile of Fig. 13 for different values of f. The dark band arises from the shell/ice interface and fills in from refractive blurring as f increases, while the Cu-doped Be zones eventually give rise to bright bands.

Figure 16: Simulated radiographs through the density profile of Fig. 13 for different, larger values of f. The wide dark band that eventually emerges as f increases is caused by the entire shell, and all fine structure is lost to refractive blurring. This is also reproduced by a diffraction calculation (bottom).

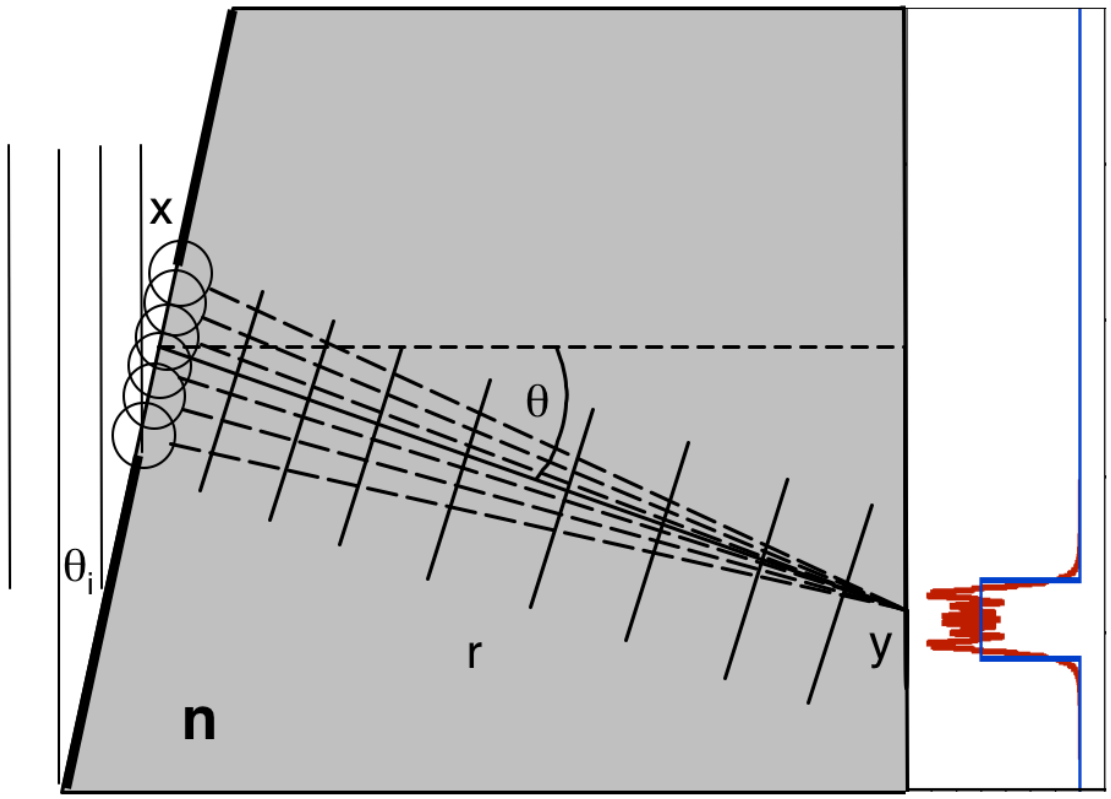
x
θ
θi
r
y
n

Figure 1

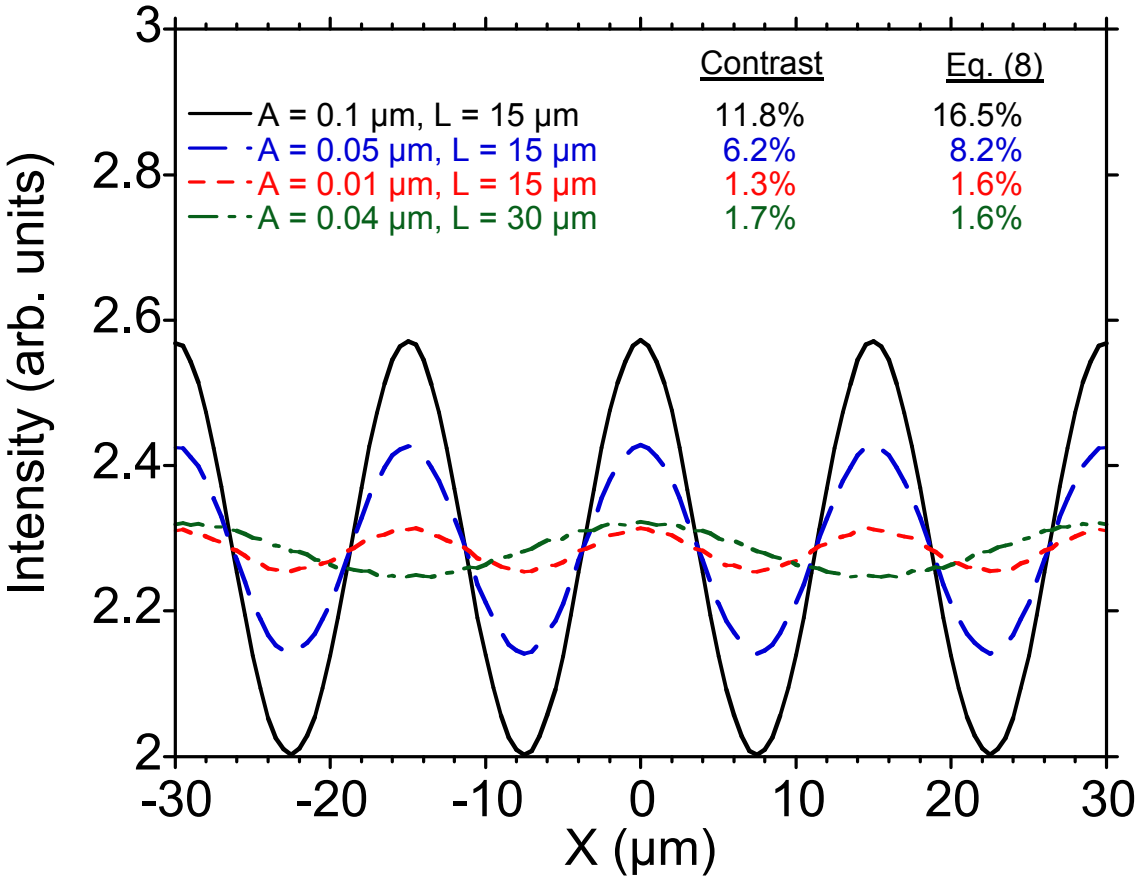
Contrast
Eq. (8)
A = 0.1 μm, L = 15 μm
11.8%
16.5%
A = 0.05 μm, L = 15 μm
6.2%
8.2%
A = 0.01 μm, L = 15 μm
1.3%
1.6%
A = 0.04 μm, L = 30 μm
1.7%
1.6%
Intensity (arb. units)
X (μm)
3
2.8
2.6
2.4
2.2
2
-30
-20
-10
0
10
20
30

Figure 2

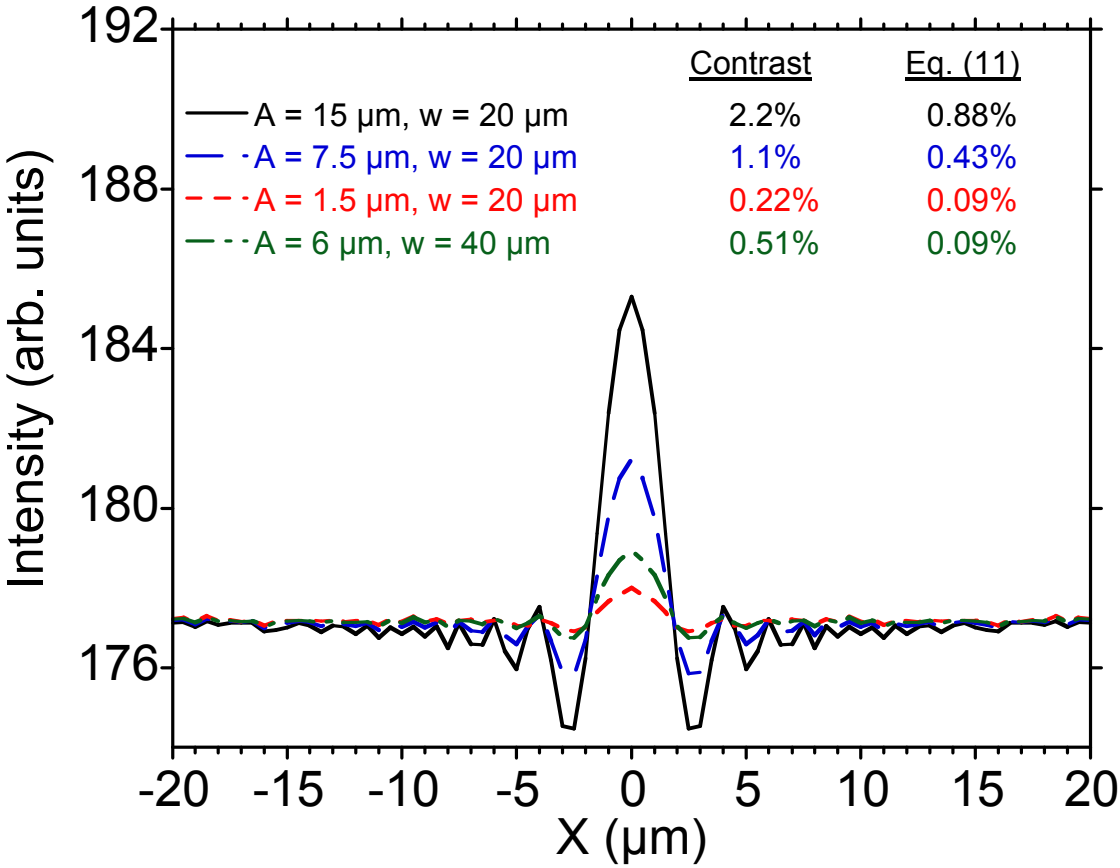
Contrast
Eq. (11)
A = 15 μm, w = 20 μm
2.2%
0.88%
A = 7.5 μm, w = 20 μm
1.1%
0.43%
A = 1.5 μm, w = 20 μm
0.22%
0.09%
A = 6 μm, w = 40 μm
0.51%
0.09%
Intensity (arb. units)
192
188
184
180
176
-20
-15
-10
-5
0
5
10
15
20
X (μm)

Figure 3

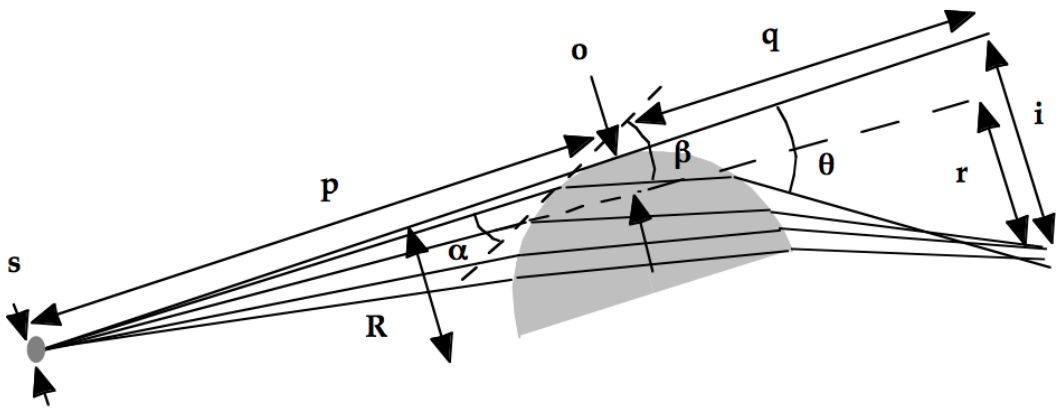

Figure 4

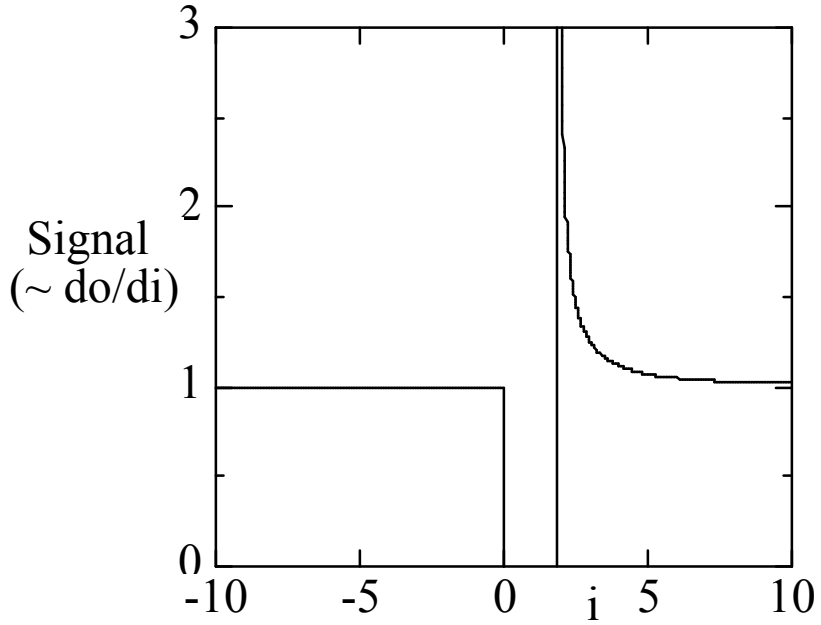

Figure 5

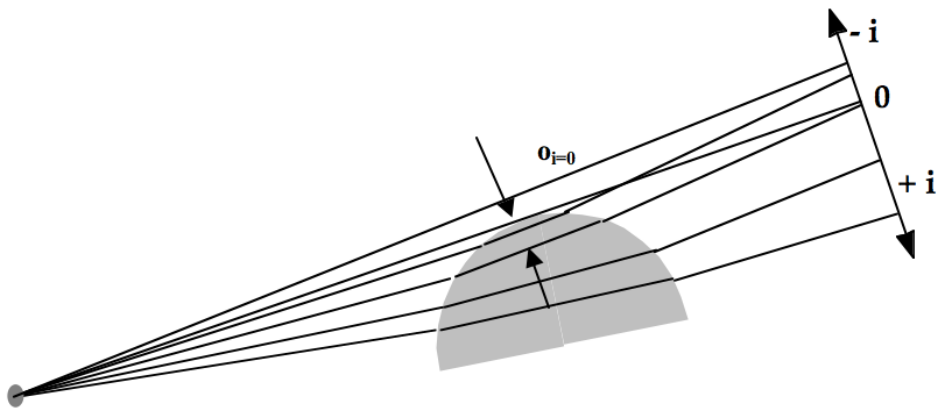

Figure 6

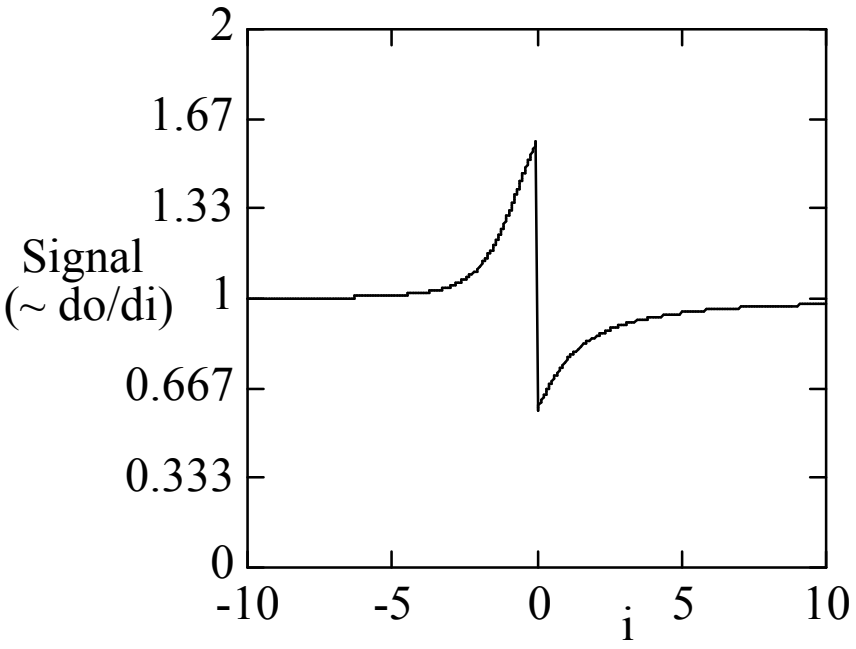

Figure 7

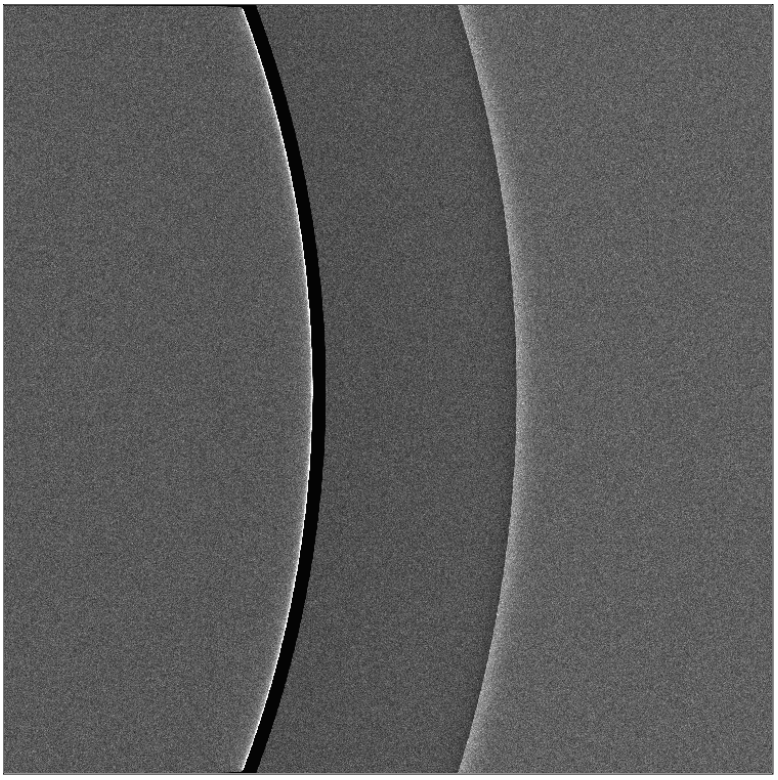

Figure 8

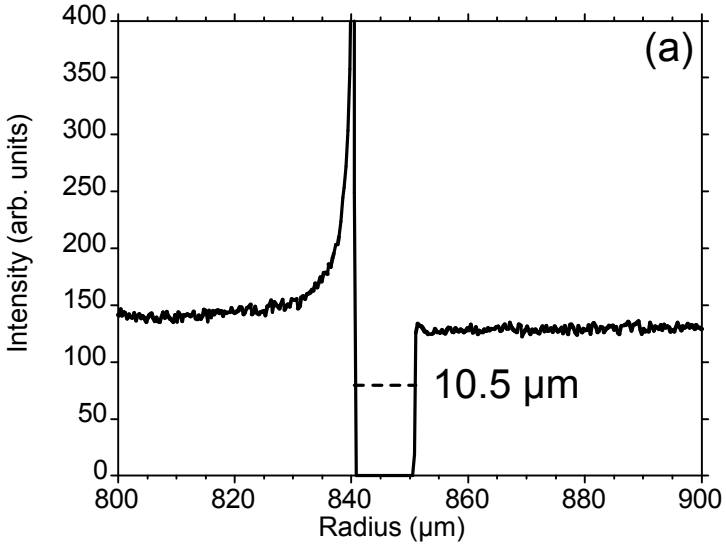
(a)
10.5 μm
Intensity (arb. units)
Radius (μm)
400
350
300
250
200
150
100
50
0
800
820
840
860
880
900

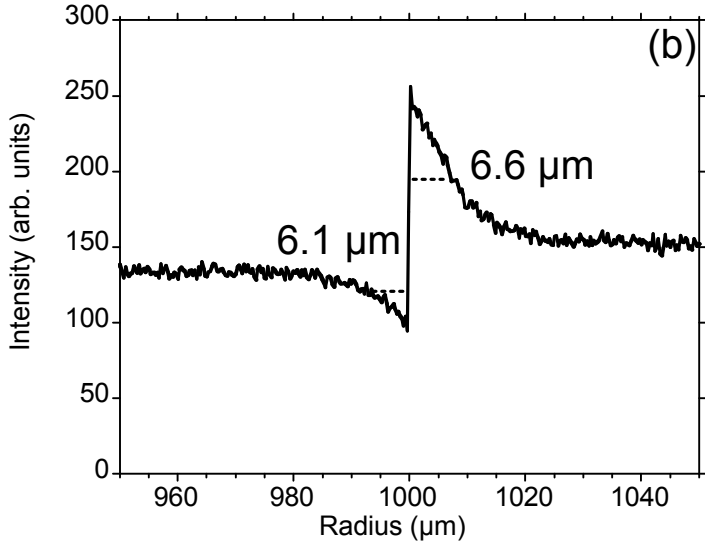
(b)
6.1 μm
6.6 μm
Intensity (arb. units)
Radius (μm)
300
250
200
150
100
50
0
960
980
1000
1020
1040

Figure 9

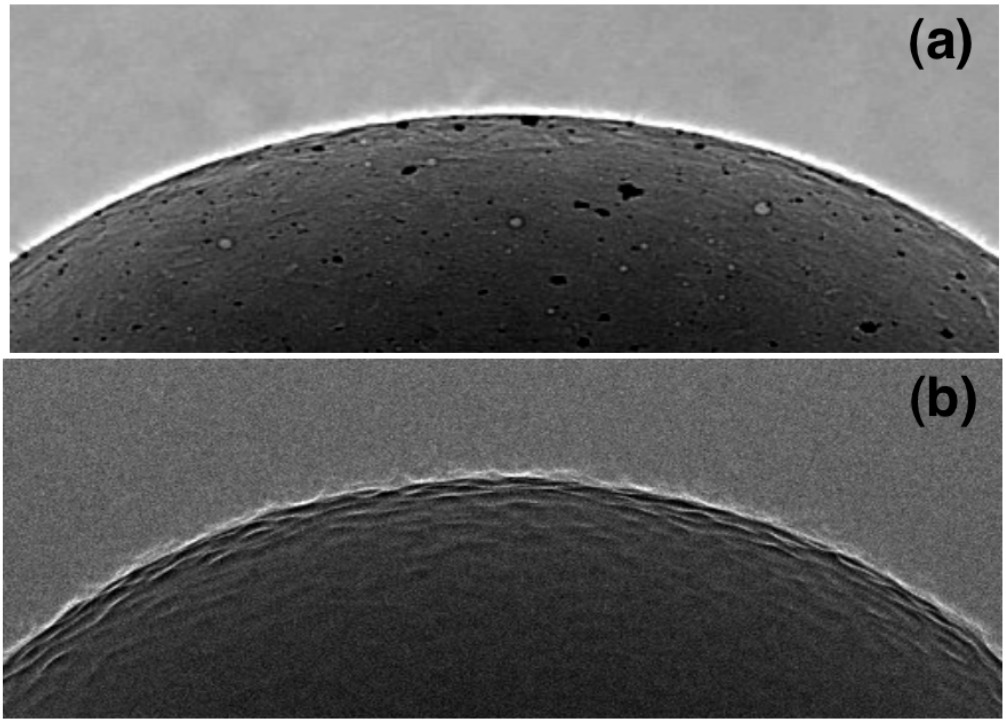
(a)
(b)

Figure 10

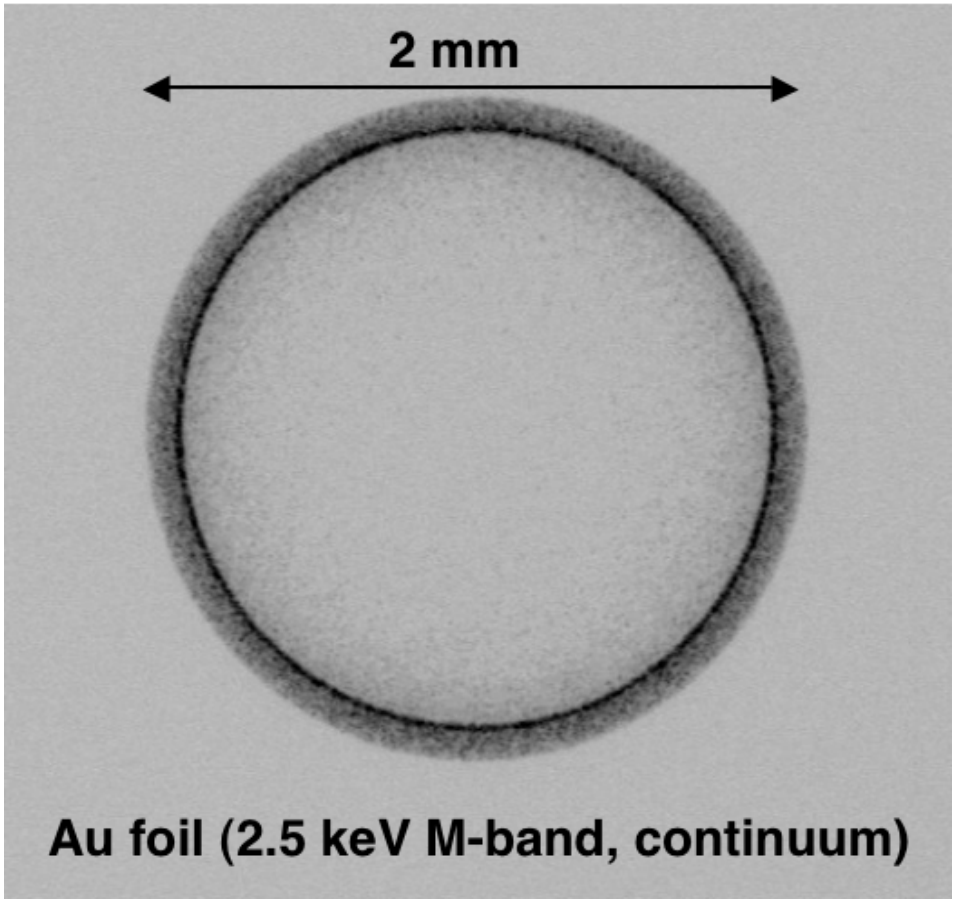

Figure 11

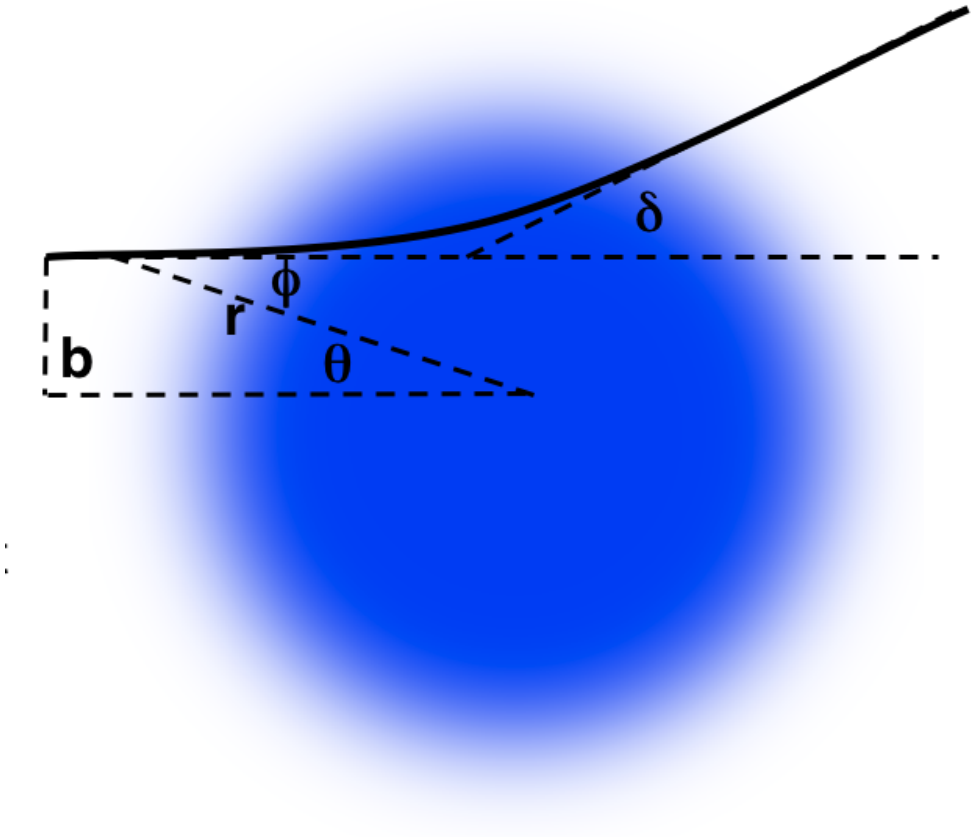

Figure 12

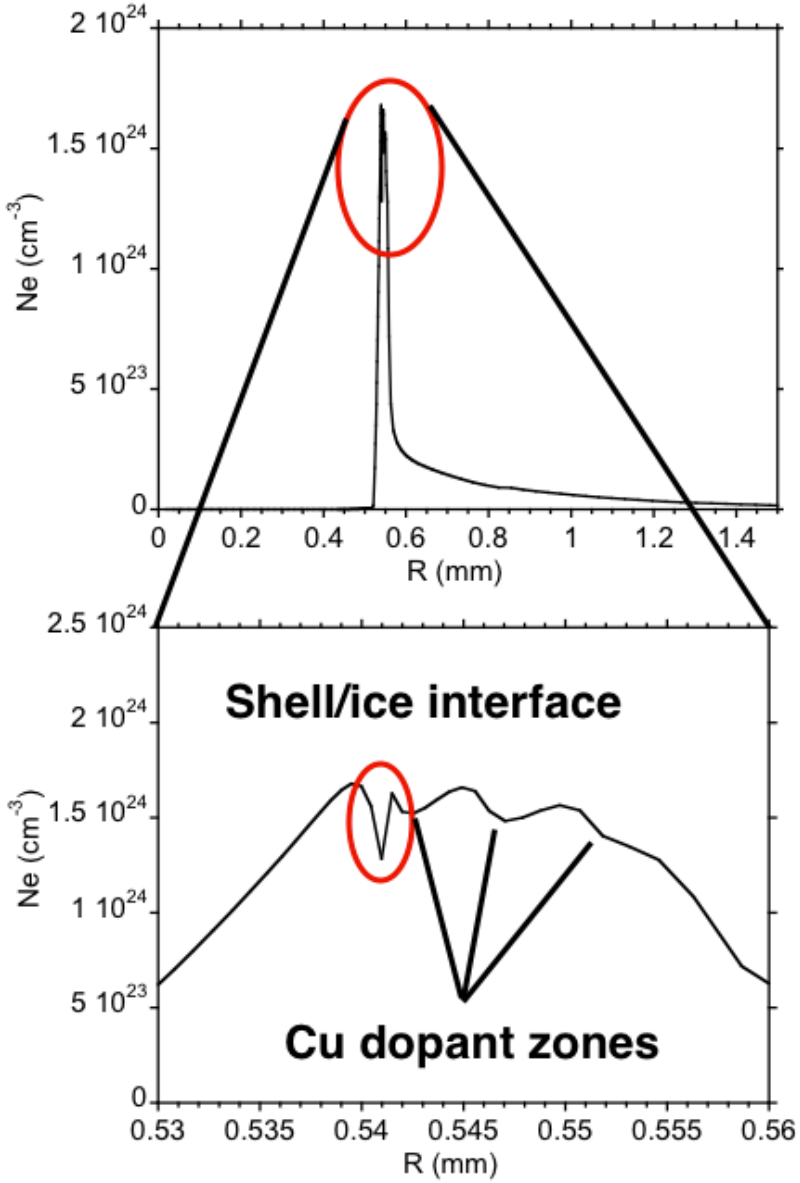
2 10^24
1.5 10^24
1 10^24
5 10^23
0
Ne (cm^-3)
0
0.2
0.4
0.6
0.8
1
1.2
1.4
R (mm)
2.5 10^24
2 10^24
1.5 10^24
1 10^24
5 10^23
0
Ne (cm^-3)
Shell/ice interface
Cu dopant zones
0.53
0.535
0.54
0.545
0.55
0.555
0.56
R (mm)

Figure 13

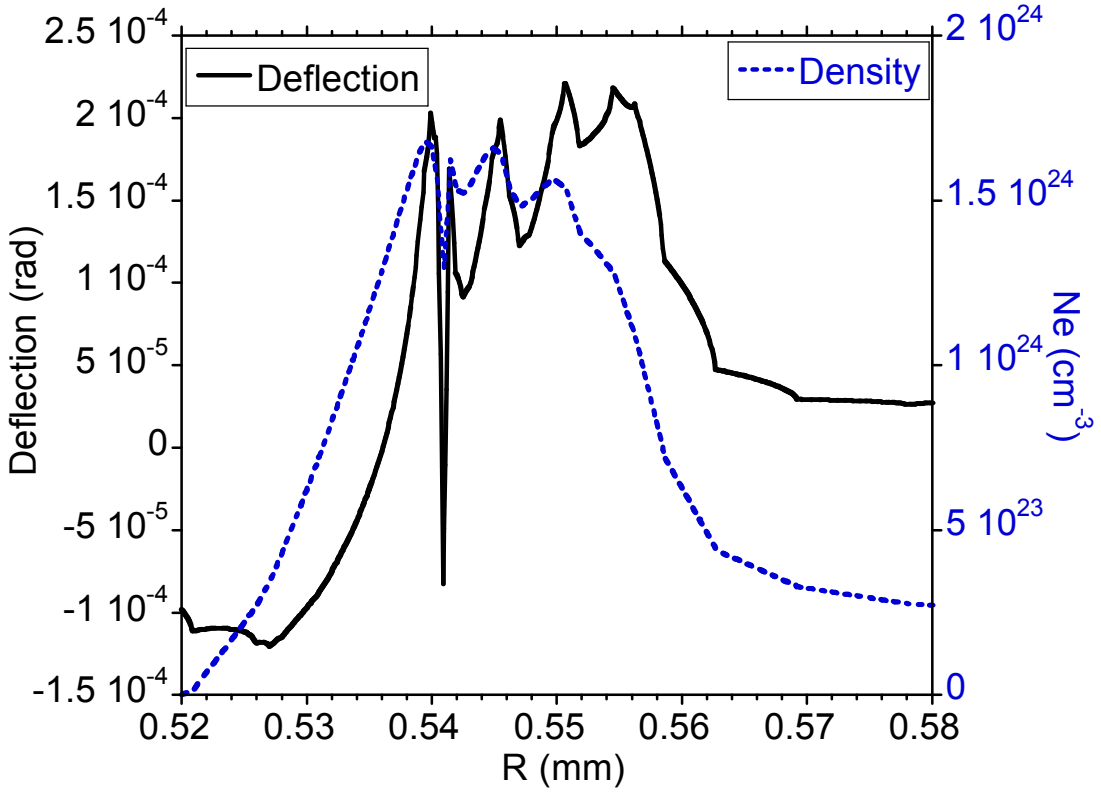
Deflection
Density
Deflection (rad)
Ne (cm-3)
R (mm)
2.5 10-4
2 10-4
1.5 10-4
1 10-4
5 10-5
0
-5 10-5
-1 10-4
-1.5 10-4
2 1024
1.5 1024
1 1024
5 1023
0
0.52
0.53
0.54
0.55
0.56
0.57
0.58

Figure 14

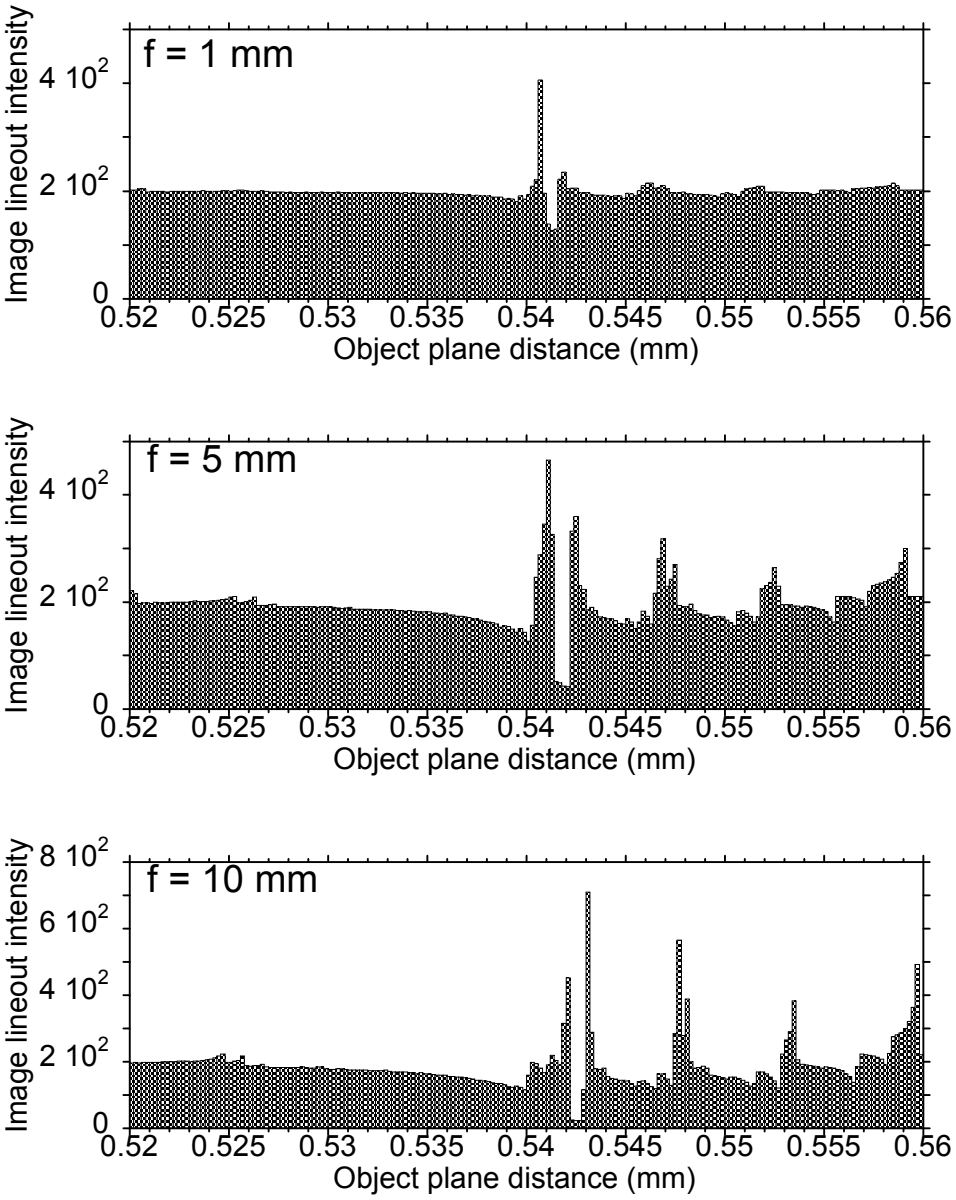
f = 1 mm
Image lineout intensity
4 10^2
2 10^2
0
0.52 0.525 0.53 0.535 0.54 0.545 0.55 0.555 0.56
Object plane distance (mm)
f = 5 mm
Image lineout intensity
4 10^2
2 10^2
0
0.52 0.525 0.53 0.535 0.54 0.545 0.55 0.555 0.56
Object plane distance (mm)
f = 10 mm
Image lineout intensity
8 10^2
6 10^2
4 10^2
2 10^2
0
0.52 0.525 0.53 0.535 0.54 0.545 0.55 0.555 0.56
Object plane distance (mm)

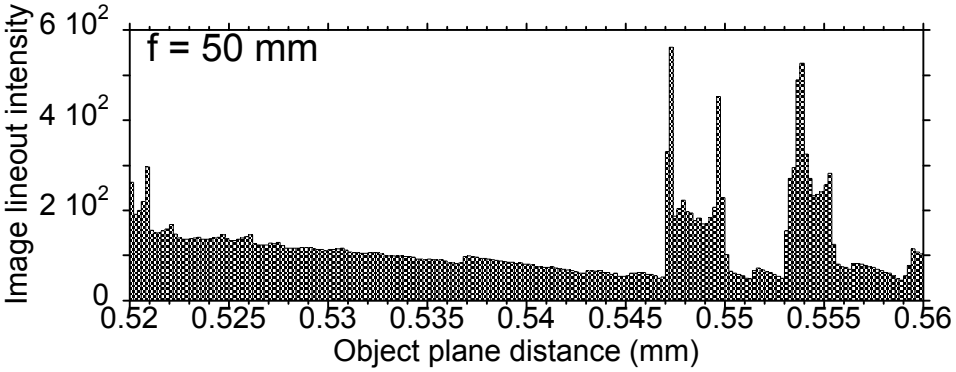
f = 50 mm
Image lineout intensity
6 10^2
4 10^2
2 10^2
0
0.52
0.525
0.53
0.535
0.54
0.545
0.55
0.555
0.56
Object plane distance (mm)

Figure 15

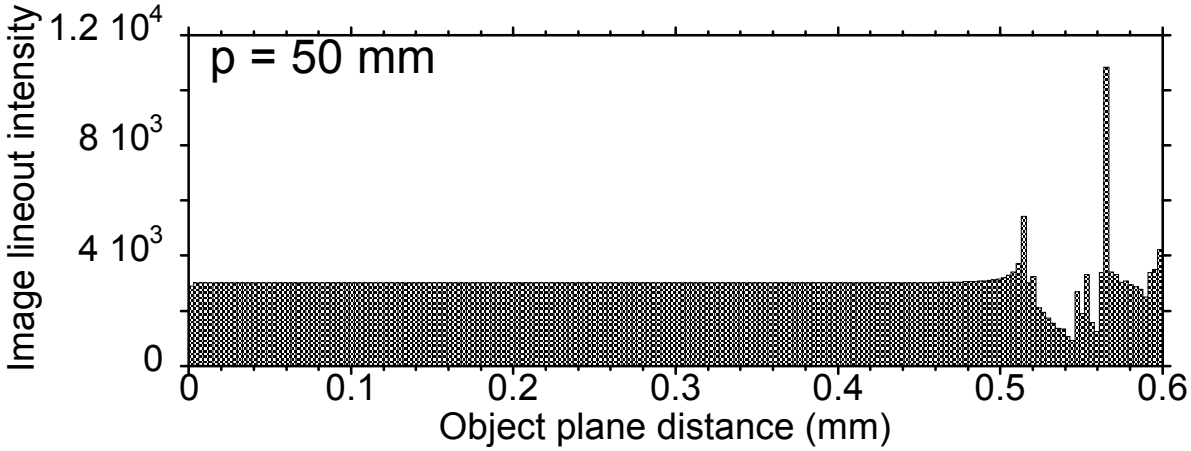
p = 50 mm
Image lineout intensity
1.2 10^4
8 10^3
4 10^3
0
0
0.1
0.2
0.3
0.4
0.5
0.6
Object plane distance (mm)

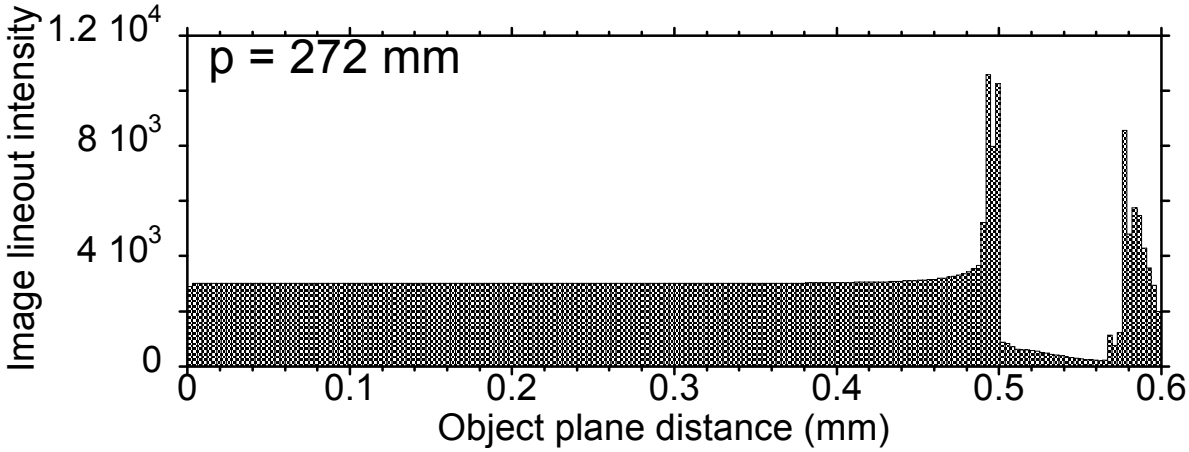
p = 272 mm
Image lineout intensity
1.2 10^4
8 10^3
4 10^3
0
0
0.1
0.2
0.3
0.4
0.5
0.6
Object plane distance (mm)

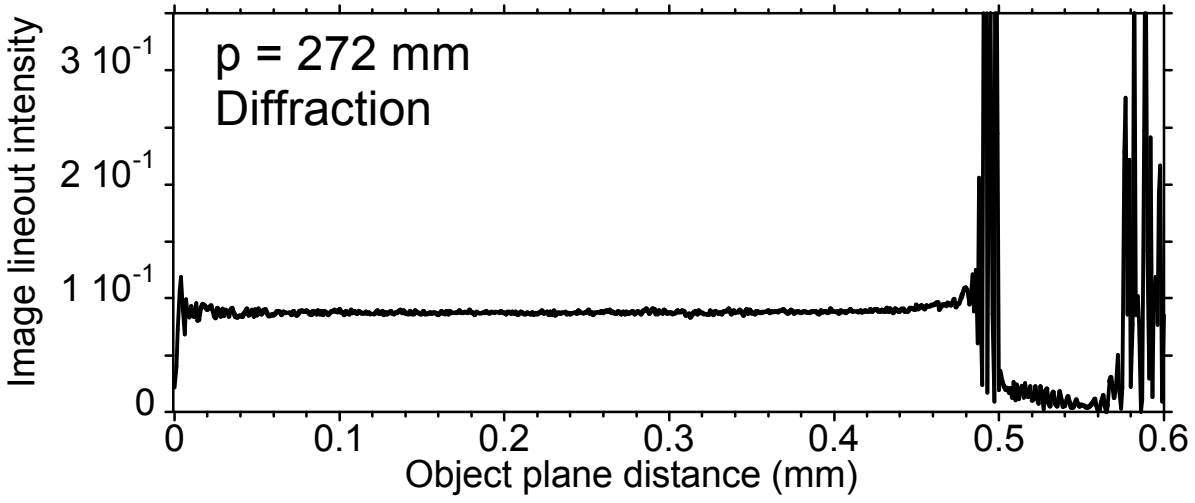
p = 272 mm
Diffraction
Image lineout intensity
3 10-1
2 10-1
1 10-1
0
0
0.1
0.2
0.3
0.4
0.5
0.6
Object plane distance (mm)

Figure 16